10-28-2009

Ion observations from geosynchronous orbit as a proxy for ion cyclotron wave growth during storm times

L. W. Blum

E. A. MacDonald

S. P. Gary

M. F. Thomsen

Harlan E. Spence
Boston University, harlan.spence@unh.edu

Recommended Citation
Blum, L. W., E. A. MacDonald, S. P. Gary, M. F. Thomsen, and H. E. Spence (2009), Ion observations from geosynchronous orbit as a proxy for ion cyclotron wave growth during storm times, J. Geophys. Res., 114, A10214, doi:10.1029/2009JA014396.

Ion observations from geosynchronous orbit as a proxy for ion cyclotron wave growth during storm times

Lauren W. Blum,[1,2] Elizabeth A. MacDonald,[2] S. Peter Gary,[2] Michelle F. Thomsen,[2] and Harlan E. Spence[1]

Received 29 April 2009; revised 27 July 2009; accepted 6 August 2009; published 28 October 2009.

[1] There is still much to be understood about the processes contributing to relativistic electron enhancements and losses in the radiation belts. Wave particle interactions with both whistler and electromagnetic ion cyclotron (EMIC) waves may precipitate or accelerate these electrons. This study examines the relation between EMIC waves and resulting relativistic electron flux levels after geomagnetic storms. A proxy for enhanced EMIC waves is developed using Los Alamos National Laboratory Magnetospheric Plasma Analyzer plasma data from geosynchronous orbit in conjunction with linear theory. In a statistical study using superposed epoch analysis, it is found that for storms resulting in net relativistic electron losses, there is a greater occurrence of enhanced EMIC waves. This is consistent with the hypothesis that EMIC waves are a primary mechanism for the scattering of relativistic electrons and thus cause losses of such particles from the magnetosphere.

Citation: Blum, L. W., E. A. MacDonald, S. P. Gary, M. F. Thomsen, and H. E. Spence (2009), Ion observations from geosynchronous orbit as a proxy for ion cyclotron wave growth during storm times, *J. Geophys. Res.*, *114*, A10214, doi:10.1029/2009JA014396.

1. Introduction

[2] The Earth's radiation belts are highly variable, and the processes contributing to their enhancement and reduction are an area of active research. High relativistic electron flux levels are found following some geomagnetic storms but not others. The resultant flux does not seem to be correlated to the size of the storm or the prestorm flux level [*Reeves et al.*, 2003]. Both acceleration and loss processes contribute to determining the poststorm populations, with wave-particle interactions believed to play an important role in these processes. *MacDonald et al.* [2008] examined whistler waves using a proxy based on the electron population and a superposed epoch analysis to find that storms resulting in higher radiation belt fluxes had higher levels of whistler waves. Their analysis agreed well with a similar superposed epoch analysis of whistler wave distributions using ground-based magnetometers [*Smith et al.*, 2004]. In this paper, we focus on electromagnetic ion cyclotron (EMIC) waves, which are often produced by the Alfven cyclotron instability driven by the anisotropy of hot plasma sheet ions [e.g., *Anderson et al.*, 1996] and can resonate with relativistic electrons to cause pitch angle scattering and thus losses to the atmosphere [*Albert*, 2003; *Summers and Thorne*, 2003].

[3] EMIC waves have long been observed in space and from the ground. In general, they have been found to be most prevalent in the dusk or afternoon sector [*Fraser and Nguyen*, 2001]. Ground observations of Pc1-Pc2 waves have indicated consistent local-time distribution; however, differences (possibly due to ionospheric attenuation) appear when comparing by storm phase; in particular, a distinct lack of these waves is observed during the storm main phase [*Engebretson et al.*, 2008]. This contrasts with most in situ observations, including early work by *Bossen et al.* [1976], which observed an increase in afternoon sector Pc1 events at geosynchronous orbit, believed to indicate EMIC waves, coinciding with the main phase of geomagnetic storms. Observational evidence for the scattering and loss of relativistic electrons by EMIC waves has been reviewed by *Millan and Thorne* [2007]. *Spasojevic et al.* [2004] used multiple IMAGE observations to show the first direct link between a detached subauroral proton arc and a plasmaspheric plume and that instability growth calculations were consistent with the Alfven cyclotron instability causing EMIC waves and proton precipitation within the plume region.

[4] In this paper we do not use direct observations of EMIC waves. Rather, we infer the existence of the waves from the observed properties of the hot plasma population using statistical analysis and linear theory, described in section 2. We develop a proxy for enhanced EMIC waves on the basis of in situ plasma parameters measured at geosynchronous orbit, and we explore the inferred occurrence of such waves relative to relativistic electron flux levels during and after geomagnetic storms.

2. Linear Theory

[5] Observations, theory, and simulations have established the following general picture for the interaction of anisotropic ion velocity distributions and enhanced EMIC fluctuations in space plasmas. Consider an idealized electron-proton collisionless plasma in which both species are represented by

[1] Astronomy Department, Boston University, Boston, Massachusetts, USA.
[2] Los Alamos National Laboratory, Los Alamos, New Mexico, USA.

0148-0227/09/2009JA014396

bi-Maxwellian velocity distributions. Consider the condition $T_{\perp p}/T_{\|p} > 1$, where the directional subscripts represent directions relative to the background magnetic field and p denotes protons. If this anisotropy is sufficiently large, it will excite growth of the electromagnetic proton cyclotron anisotropy instability [*Gary*, 1993]. The resulting enhanced EMIC fluctuations have maximum growth at $\mathbf{k} \times \mathbf{B}_0 = 0$, where $\mathbf{B}_0$ is the background magnetic field and $\mathbf{k}$ is the wave vector, with a range of frequencies $0 < \omega < \Omega_p$, where the latter symbol represents the proton cyclotron frequency. The fluctuations from this instability are further characterized by left-hand polarization and weak magnetic compressibility.

[6] The enhanced fluctuations are resonant with and scatter the protons so as to reduce $T_{\perp p}/T_{\|p}$ and thereby quench the instability. As a result an upper bound is imposed upon the proton anisotropy, which can be written as

$$\frac{T_{\perp p}}{T_{\|p}} - 1 = \frac{S_p}{\beta_{\|p}^{\alpha_p}}, \tag{1}$$

where $\beta_{\|p} = 8\pi n_p T_{\|p}/B_0^2$ and S_p and α_p are parameters which are obtained by a fit to the instability threshold condition derived from linear theory. For example, choosing the maximum growth rate to be $\gamma_m/\Omega_p = 10^{-3}$ yields $S_p = 0.43$ and and $\alpha_p = 0.42$ for a fit over the range $0.01 \leq \beta_{\|p} \leq 10$ [*Gary et al.*, 1994].

[7] In the terrestrial magnetosphere, observations show the existence of two or more distinct components in ion velocity distributions. Consider the idealized picture of two proton components, one hot (h) and one cool (c). In the plasmasphere, $n_c \gg n_h$ and $T_{\|h} \gg T_{\|c}$; the cool component is relatively dense and collisional so that it is relatively isotropic. Beyond the plasmasphere, the cool component persists but at densities such that $n_c \sim n_h$. The presence of the cool component modifies the properties of the proton cyclotron instability so that the upper bound on the anisotropy is written as

$$\frac{T_{\perp h}}{T_{\|h}} - 1 = \frac{S_h}{\beta_{\|h}^{\alpha_h}}, \tag{2}$$

where $\beta_{\|h} = 8\pi n_h T_{\|h}/B_0^2$ and S_h and α_h are fitting parameters which are functions of both γ_m/Ω_p and n_h/n_e, where n_e is the electron density, which we take to be equal to $n_h + n_c$ [*Gary et al.*, 1994]. Equation (2) has the same form as (1), namely that of a limiting temperature anisotropy, though the limit to the instability now has a more complex description. If we choose a fixed value of the maximum growth rate, we can then use linear theory to determine how these two fitting parameters vary with the relative hot proton density. Linear theory shows that both parameters are relatively weak functions of n_h/n_e. We have quantified this result by choosing the forms

$$S_h = \sigma_0 + \sigma_1 \ln(n_h/n_e) + \sigma_2[\ln(n_h/n_e)]^2 \tag{3a}$$

$$\alpha_h = a_0 - a_1 \ln(n_h/n_e) - a_2[\ln(n_h/n_e)]^2. \tag{3b}$$

Then, assuming $\gamma_m/\Omega_p = 10^{-3}$, we fit linear theory results to these two curves, obtaining $\sigma_0 = 0.429$, $\sigma_1 = 0.124$, $\sigma_2 = 0.0118$, $a_0 = 0.409$, $a_1 = 0.0145$, and $a_2 = 0.00028$.

[8] The most direct determination of EMIC wave activity in space plasmas is through the use of spacecraft magnetometers, which measure the level of magnetic fluctuations near and below the proton cyclotron frequency. However, the plasma data described in section 3 are obtained from spacecraft that do not carry magnetometers; thus, we have developed a procedure, similar to *MacDonald et al.* [2008] for whistler waves, whereby theory and plasma observations become a proxy for direct measurements of wave activity.

[9] The procedure is as follows. We define the observational EMIC parameter

$$\Sigma_h = \left(\frac{T_{\perp h}}{T_{\|h}} - 1\right)\beta_{\|h}^{\alpha_h}. \tag{4}$$

Here $T_{\|h}$, $T_{\perp h}$ and n_h are measured by the plasma instrument, α_h is determined via equation (3b) using measured values of n_h/n_e, and the background magnetic field B_0 necessary to calculate $\beta_{\|h}$ is taken from the T89 magnetic field model. Then if we plot experimental values of Σ_h as a function of the relative hot proton density, those values can be compared against the theoretical expression for the threshold S_h given as equation (3a). If $\Sigma_h < S_h$ for a measurement time interval, it is likely that the hot protons are not sufficiently anisotropic to excite the Alfven cyclotron instability at the prescribed growth rate. In contrast, if the observations yield $\Sigma_h > S_h$, it is likely that this mode is unstable during the measurement. Thus, a comparison of the two quantities becomes a proxy for determining the level of enhanced EMIC wave activity. We expect that the choice of an appropriate value of the maximum growth rate will yield an $S_h(n_h/n_e)$ which provides a statistical upper bound on the observed Σ_h. The growth rate needed to bound the observed anisotropies should be an indication of how strongly the instability is driven.

3. Observations

[10] In this study, we use Los Alamos National Laboratory (LANL) Magnetospheric Plasma Analyzer (MPA) particle data to develop the proxy for enhanced EMIC wave activity, Σ_h, from equation (4). We look at data from seven satellites at geosynchronous orbit from years 1989–2004. We calculate bulk moments, including density and perpendicular and parallel temperature for both the hot proton population, defined as 100 eV to 45 keV, and the cool protons, less than 100 eV. Here perpendicular and parallel are in reference to the background magnetic field vector, as inferred from symmetry in the plasma distributions [*Thomsen et al.*, 1999]. The ion population is assumed to be only protons as the MPA instrument does not distinguish among the various ion species. While magnetospheric conditions can be quite far from this ideal, the presence of heavy ions should not greatly affect our calculations. Cold He^+ can at times constitute a significant fraction of the cold magnetospheric ions, but it does not contribute substantially to driving the instability. Although helium cyclotron damping creates a stop band in the spectrum near the helium cyclotron frequency, the maximum growth rate is only modestly reduced [*Gendrin et al.*, 1984; *Kozyra et al.*, 1984]. Hot magnetospheric O^+ can also be present during magnetic storms. Such ions can be anisotropic and can contribute to instability growth, but the resonant frequencies of such waves are near 1/16 Ω_p and

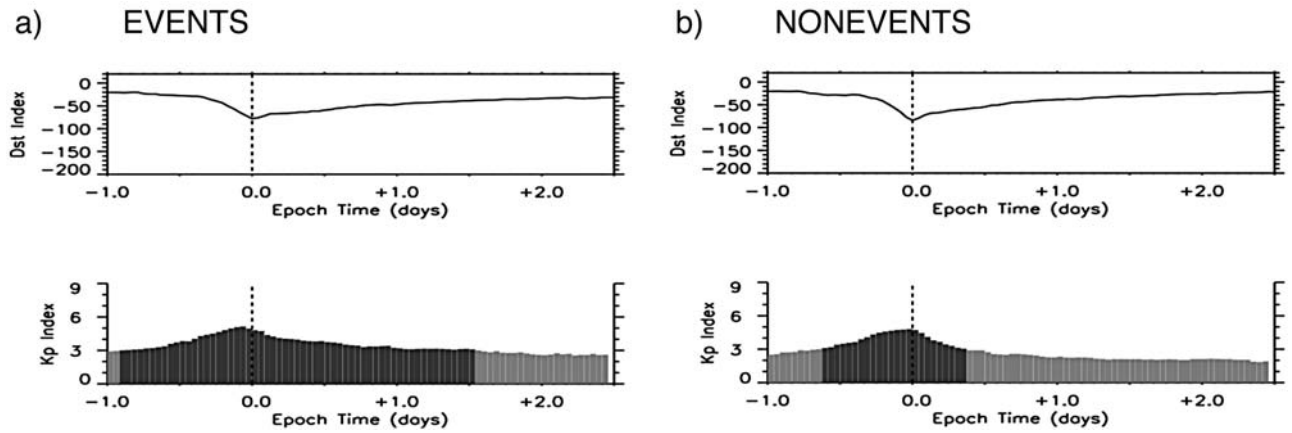

Figure 1. Plots of superposed storm *Dst* and *Kp* for "events" and "nonevents." *Dst* profiles look similar, while an elevated *Kp* (above 3) lasts about a full day longer for events.

therefore resonate with electrons of energies a few times higher than the MeV ones of primary geophysical interest [*Meredith et al.*, 2003].

[11] From these data, we use a superposed epoch technique to examine over 300 storms, chosen following criteria first described by *O'Brien et al.* [2001, 2003] and subsequently used by *Smith et al.* [2004] and *MacDonald et al.* [2008]. Storms were superposed by setting the time of minimum *Dst* equal to zero epoch. The storms were chosen to be isolated, not within 4 days of another storm's minimum *Dst*, and to have a minimum *Dst* of less than −50 nT. The storm list is divided into two categories, events and nonevents, on the basis of poststorm relativistic electron flux levels measured by LANL satellites at geosynchronous orbit. Storms whose noon-reconstructed 1.8–3.5 MeV electron flux was above 0.5 e/cm^2 s sr keV for 48–72 h after *Dst* minimum were categorized as events, and those with fluxes lower than 0.5 were categorized as nonevents. (The so-called noon reconstruction technique is described by *O'Brien et al.* [2001].) These criteria, based only on the poststorm flux, were chosen because the prestorm flux has been shown to be uncorrelated with the poststorm result [*Reeves et al.*, 2003].

[12] Figure 1 shows superposed *Dst* and *Kp* plots for both the 138 storms constituting the events list, having higher poststorm flux levels, and the 183 storms of the nonevents, having lower levels. The *Dst* profiles for the two groups of storms look fairly similar, while the *Kp* for events stays elevated, above a level of 3, for approximately 1 day longer than nonevents. This suggests that the events storms have extended driving, similar to corotating interaction region (CIR) occurrences examined using superposed epoch analysis by *Miyoshi and Kataoka* [2005] and *Denton et al.* [2006].

[13] With this data set, we compare relevant properties of the geosynchronous proton population for the events and nonevents storm lists. We examine the effect of these parameters on the enhanced EMIC wave proxy for the two sets of storms, globally and as a function of storm phase, or epoch time.

4. Results

[14] We perform an observational test of the linear theory proxy formulation discussed in section 2, and we compare the theoretical instability threshold S_h to our observational EMIC growth parameter Σ_h. The solid lines in Figure 2 show S_h as a function of the ratio of the hot proton density to the total density n_h/n_e for three different growth rates, $\gamma_m/\Omega_p = 0.001$, 0.004, and 0.01. The scatter points show Σ_h for the nonevents storm set for two different local times, at noon and at midnight. Both events and nonevents storm sets show similar qualitative behavior when plotted in this manner. Here, data points with increasing Σ_h values relative to an S_h curve correspond to the transition from stable conditions to successively stronger growth rates. Σ_h approaches a theoretical limit (e.g., $\gamma_m/\Omega_p = 0.01$ for the noon points) indicating that enhanced fluctuations from the EMIC instability are effectively scattering protons near this threshold condition and are imposing a statistical constraint on the proton temperature anisotropy. Figure 2 validates the use of the observed Σ_h compared to the theoretical limit of S_h as a proxy for enhanced EMIC waves. Additionally, it tells us that a growth rate of 0.001 is appropriate for data points at midnight, while a higher value of 0.01 is approached during local times around noon.

[15] We plot various parameters over local and epoch times to better understand the variations of constituent plasma properties for our events and nonevents storm sets. We begin by looking at the different density components of the proton population, the hot and cool, as well as the ratio of the hot to total proton density n_h/n_e (Figures 3a, 3c, and 3e for events and Figures 3b, 3d, and 3f for nonevents). Figures 3a and 3b show the hot plasma sheet density, highest around minimum *Dst* from dusk through dawn, extending further both in local and epoch time for the nonevents storms, as seen by *Denton et al.* [2006]. In Figures 3c and 3d, there is evidence of cold dense plasmaspheric plumes in the afternoon sector during storm main phase (prior to minimum *Dst*) and continuing, with a weaker presence and narrower in local time, through the recovery phase in both sets of storms. The density ratio (Figures 3e and 3f) is a variable when calculating S_h that affects the value of the instability threshold for a given growth rate (see Figure 2). Over most of the range of n_h/n_e, a lower ratio (corresponding to more cool plasma) lowers the instability threshold, and enhanced EMIC waves can more easily be obtained. Both Figures 3e and 3f show that the plasma sampled at geosynchronous orbit is dominated by hot

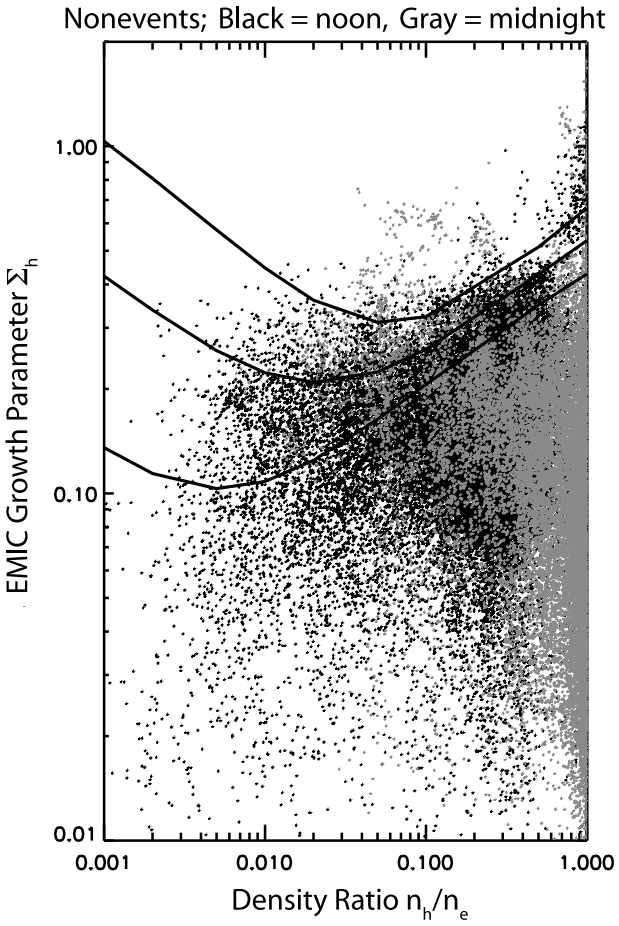

Figure 2. Scatterplot of EMIC growth parameter Σ_h versus the density ratio n_h/n_e (hot proton density divided by total proton density) for noon (black points) and midnight (gray points) for the nonevents storm set. The instability threshold S_h is also plotted here as three solid black lines, corresponding to three different growth rates (the lowest line for a growth rate of 0.001, then 0.004, and highest is 0.01). We see the Σ_h points approach S_h of different growth rates at different local times; γ_m/Ω_p = 0.001 is appropriate for data points at midnight, while 0.01 is approached around noon.

plasma in the midnight sector throughout the duration of the storms and that very low levels of hot protons exist on the day side. Starting just prior to 1 day after minimum *Dst*, the density ratio is lower for the nonevents than events in the region around midnight.

[16] We also explore the temperature anisotropy of the hot protons for both storm lists (Figures 4a and 4b), as it is the temperature anisotropy in this population that drives the Alfven cyclotron instability responsible for the growth of EMIC mode waves. Here a difference between the events and nonevents is most striking during the recovery phase. The night-side anisotropy increases after zero epoch in the nonevents, while in the events it remains at levels around 1.0 on most of the night side.

[17] Figures 4c and 4d show the hot proton parallel beta $\beta_{\|h}$ for events and nonevents. Beta is composed of the hot proton density as well as the hot parallel temperature. The combination of these parameters makes for slightly higher beta levels in the nonevents, but the similar profiles suggest that this parameter does not cause significant differences between events and nonevents in the observational EMIC growth parameter Σ_h.

[18] In Figure 5, we plot the theoretical instability threshold S_h, as well as the observational EMIC growth parameter Σ_h, for events and nonevents. Here we use a growth rate of 0.001, as suggested by Figure 2, to calculate S_h. Figures 5a and 5b show that S_h has the same variation pattern as n_h/n_e (from Figures 3e and 3f) since the density ratio is the only plasma parameter upon which S_h depends. Figures 5a and 5b show variation of the instability threshold S_h over local and epoch times, but the difference between storm sets does not appear to be great.

[19] The observational EMIC growth parameter Σ_h (Figures 5c and 5d), however, shows a significant difference between the events and nonevents storm sets, as well as a great deal of variation over local time. Nonevents have a higher value, especially around noon, but additionally around dawn in the recovery phase. The absolute value of this parameter alone, though, is not necessarily indicative of higher wave growth, but must be compared with the expected S_h at given local and epoch times to be able to infer relative wave growth.

[20] To make this comparison, we calculate the percent of Σ_h data points that exceed the average S_h for each local and epoch time bin. Figure 6 shows the percentage of time that the observational EMIC growth parameter Σ_h exceeds the average instability threshold for a growth rate of 0.001. Here we see that the percentage is high for both events and nonevents in the day leading up to minimum *Dst*, but it remains elevated longer during the period of 1 to 4 days after minimum *Dst* for the nonevents.

5. Discussion

[21] Figure 7 shows the epoch time dependence of this percentage averaged from noon to dusk, the region of most interest. Here gray indicates nonevents, black indicates events, and the thin solid line shows the quiet time average of both storm sets (from 6 to 10 days after storm epoch), with dotted lines showing the standard deviation averaged for both storm sets. The events storms, which result in elevated relativistic flux levels 48 to 72 h after minimum *Dst*, show different Σ_h behavior than the nonevents especially 1 to 4 days after zero epoch, during the recovery phase of the storms. Both types of storms appear to have higher occurrence of enhanced EMIC waves, according to our proxy, in the main phase of the storm, which is consistent with in situ wave measurements seen by B. J. Fraser et al. (Stormtime observations of electromagnetic ion cyclotron waves at geosynchronous orbit: GOES results, submitted to *Journal of Geophysical Research*, 2009). They then both display a sharp drop in this measurement immediately after zero epoch, minimum *Dst*. In the subsequent days, however, the nonevents recover to levels around 8% (an average quiet time value), while the events remain at around 3%. The quiet time value for both storm sets fluctuates, with an average value around 7.5%. This suggests that the difference in events and nonevents in the recovery phase of storms is associated with a suppression of EMIC growth in the events, rather than an enhancement in the nonevents. One possible explanation for this is that CIR storms, which show similar properties to our

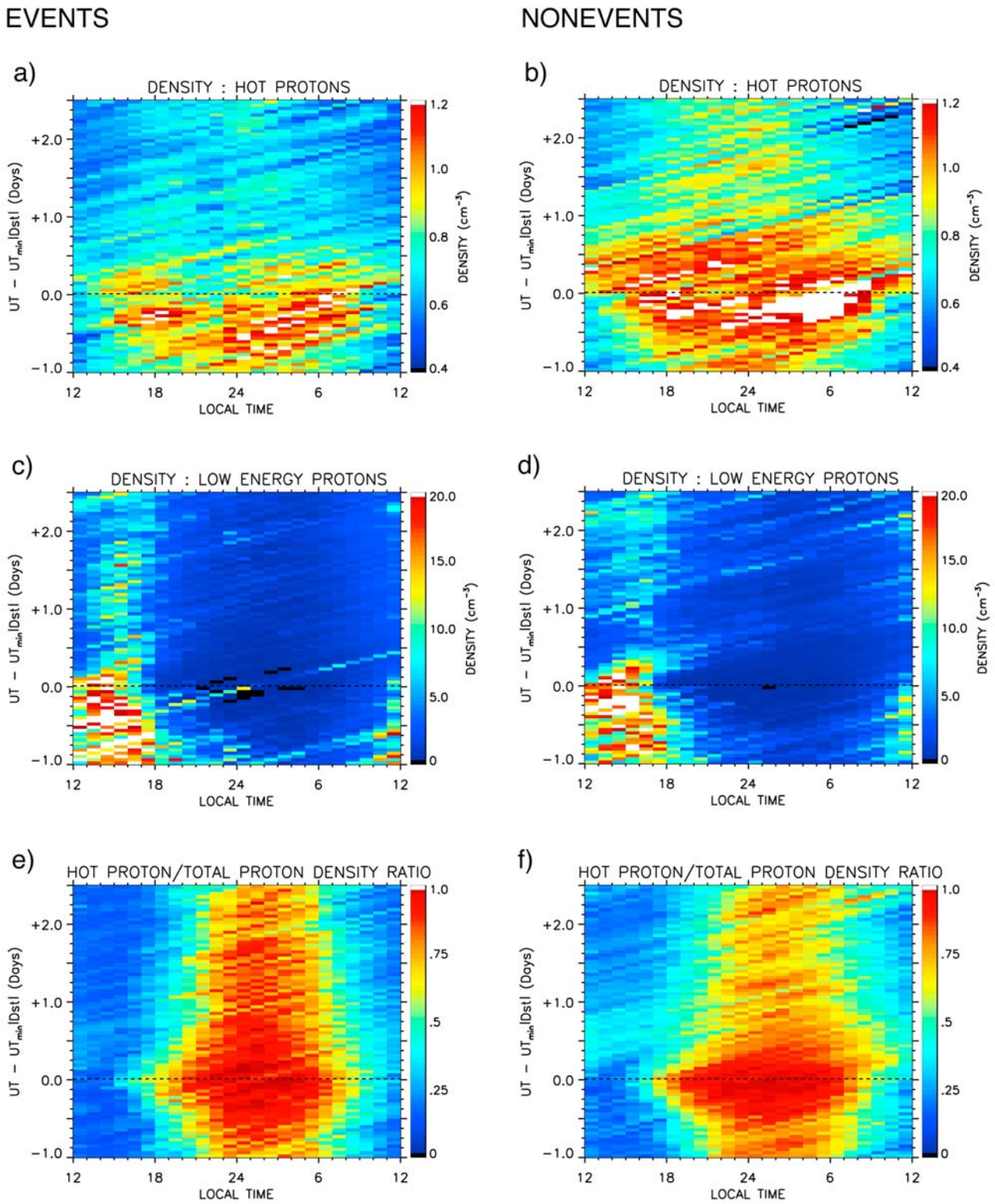

Figure 3. (a and b) Hot proton density n_h, (c and d) cold proton density n_c, and (e and f) density ratio n_h/n_e plots across all local and epoch times for events and nonevents. Density ratio n_h/n_e is lowest in the region from approximately noon to dusk, where the cold dense plume is located.

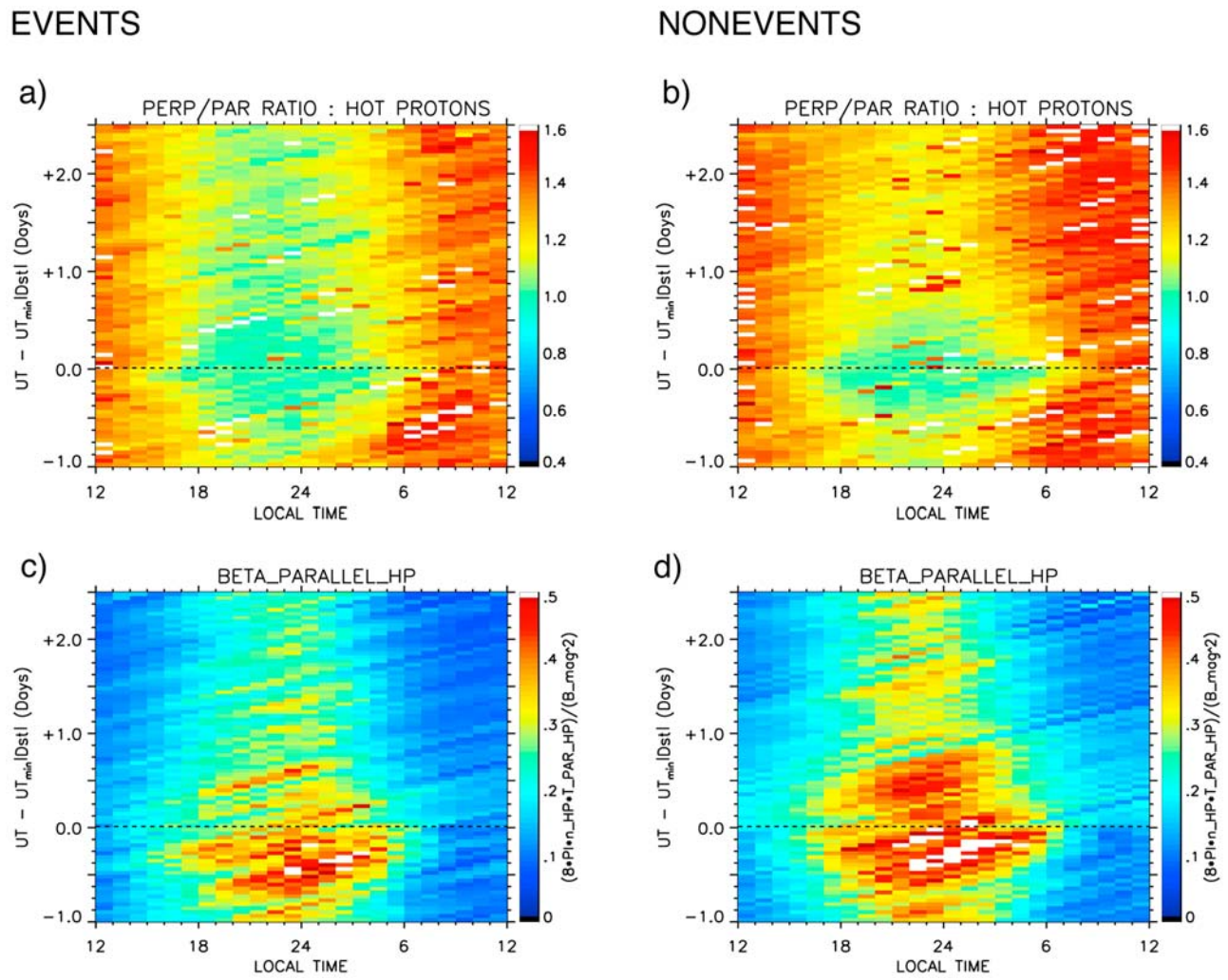

Figure 4. (a and b) Temperature anisotropy and (c and d) plasma Beta $\beta_{\|h}$ for hot proton populations. These two parameters are the main components in the calculation of the observational EMIC growth parameter Σ_h.

events storms, involve enhanced convection and elevated *Kp*. *Denton et al.* [2005] show that temperature anisotropy is typically inversely related to *Kp* index. As temperature anisotropy is a main component of our calculation of the EMIC growth parameter, a lower anisotropy could lead to suppressed Σ_h values. As *Kp* remains elevated during the recovery period of our events storms, as seen in Figure 1, less anisotropic plasma is present during this period, leading to the suppression of EMIC growth seen in our events storms.

[22] We return to Figure 6 to examine the percentage values over all local and epoch times. The most concentrated area of enhanced EMIC fluctuations is shown to be in the region from noon to dusk. This is in agreement with in situ EMIC wave observations, as shown by both *Meredith et al.* [2003] and *Bossen et al.* [1976]. The distribution of elevated values in these final percentage plots (Figure 6) differs significantly from those for the observational EMIC growth parameter Σ_h alone in Figures 5c and 5d. This emphasizes the need to compare the observed Σ_h to the theoretical instability threshold determined by S_h. While the temperature anisotropy and hot plasma beta parameters cause elevated values from dawn nearly to dusk in our nonevents, the density ratio causes the instability threshold to be more easily attained only from noon to dusk, where more cold plasma is present. Therefore, we conclude that the Alfven cyclotron instability can grow, and enhanced EMIC waves can arise, most easily from noon to dusk, showing that our proxy for such waves corresponds in local time to wave observations.

6. Summary

[23] In conclusion, we have used plasma measurements from MPA instruments at geosynchronous orbit to show that the linear threshold of the Alfven cyclotron instability is approached at certain local times. This, combined with the local time agreement seen in Figure 6, supports our examination of EMIC wave presence and distributions using plasma measurements from MPA at geosynchronous orbit. This result enables broader understanding of the powerful applications of using plasma data to infer wave distributions in space.

[24] We observe that there are differences in the statistical behavior of certain relevant plasma properties between storms resulting in higher versus lower net fluxes of relativ-

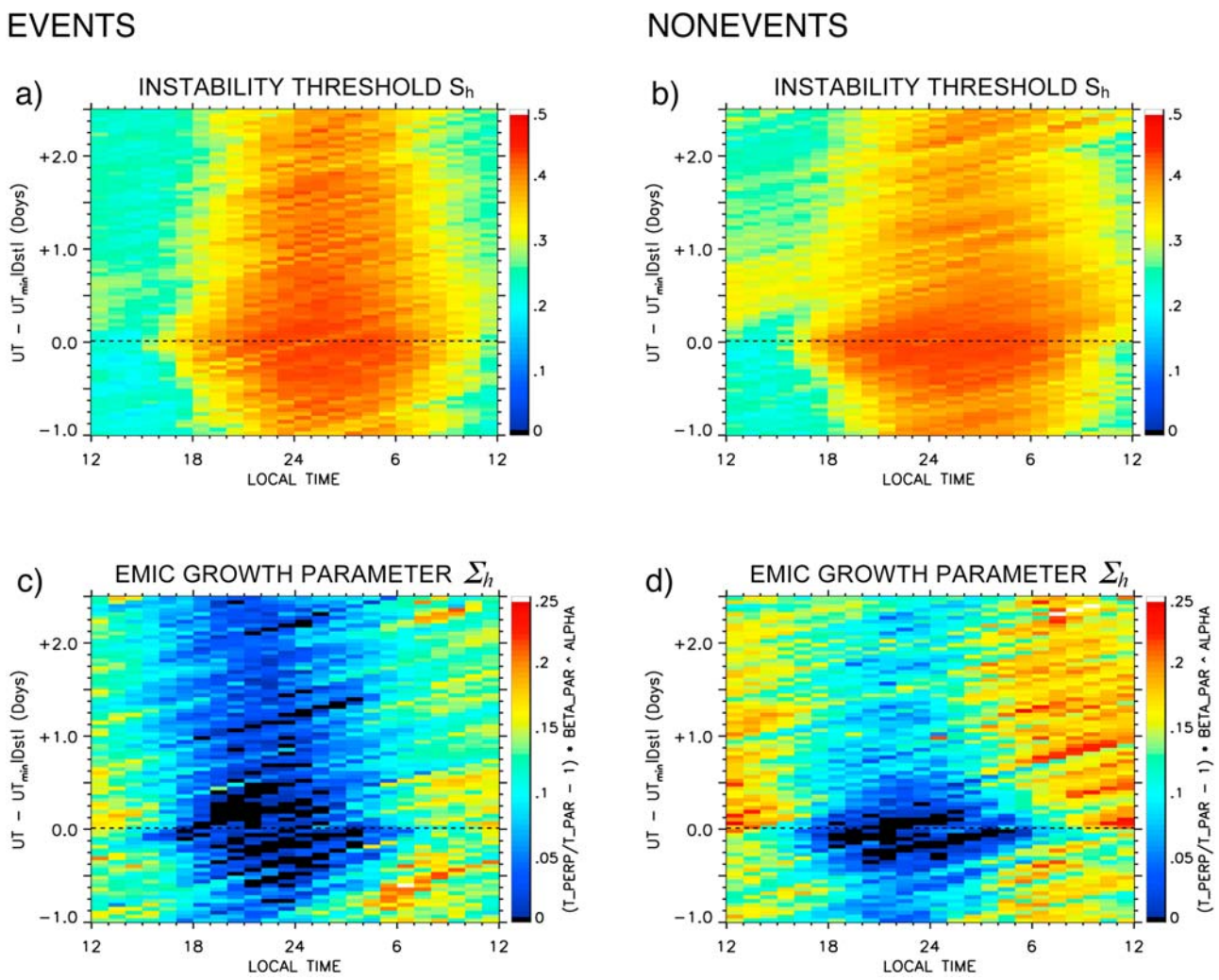

Figure 5. (a and b) Theoretical instability threshold S_h, dependent on the density ratio n_h/n_e only, and (c and d) EMIC growth parameter Σ_h, based on measured plasma parameters. Both are plotted for all local and epoch times for a growth rate $\gamma_m/\Omega_p = 0.001$.

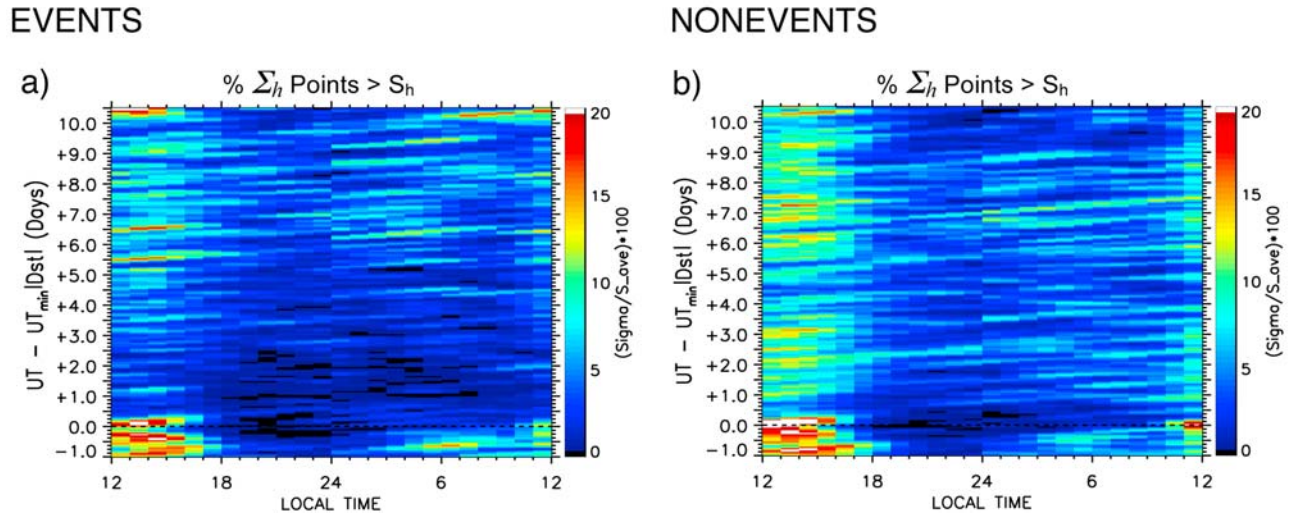

Figure 6. The percentage of Σ_h values which lie above the average S_h value for a given local and epoch time. For both (a) events and (b) nonevents, this percentage is high from noon to dusk during the main phase of the storm. In the recovery phase, however, there is a significant difference between the two storm sets, and the values for the nonevents are higher than events for a few days after minimum *Dst*.

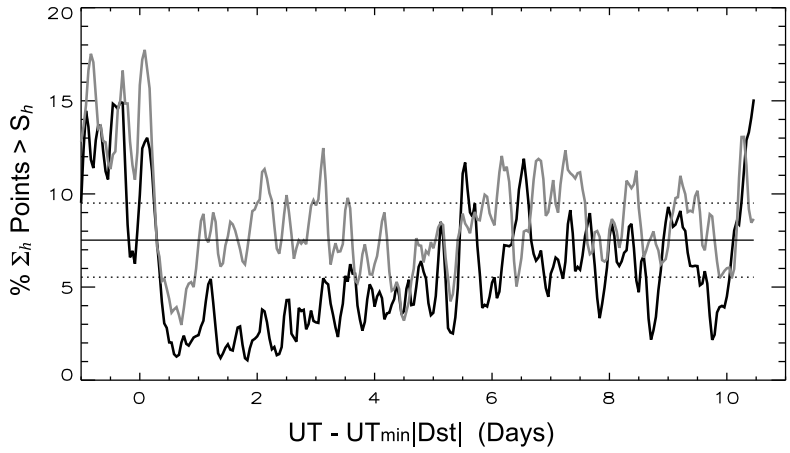

Figure 7. An average of the parameters plotted in Figure 6 taken from noon to dusk. The black line represents the events, and the gray represents the nonevents. Here the difference in the percentage between the storm sets in the recovery phase is even more distinct. The quiet time average is displayed with the thin solid line, along with the standard deviation (dotted lines).

istic electrons. From these plasma parameters and validated linear theory, we find that both the average values of our observational EMIC growth parameter Σ_h, as well as the frequency of elevated values, are greater, especially in the recovery phase of the storm, for storms resulting in lower radiation belt fluxes, labeled nonevents. Our study reveals that the percent of time that EMIC wave growth exceeds a rate of $\gamma_m/\Omega_p = 0.001$ is greater for our nonevents, which result in lower relativistic electron flux levels after storms. This is consistent with the idea that enhanced EMIC waves scatter relativistic electrons and thereby contribute to the loss of such particles from the magnetosphere in the main phase, and for nonevents on into the recovery phase, preventing the buildup of substantial poststorm flux enhancements.

[25] **Acknowledgments.** The authors would like to acknowledge a number of grants that have assisted this research. This work was supported in part by the Radiation Belt Storm Probes Energetic particle, Composition, and Thermal plasma science investigation under NASA contract award 923497. The Los Alamos portion of this work was performed under the auspices of the U.S. Department of Energy (DOE). This research was supported in part by the Solar and Heliospheric Physics SR and T and the Heliophysics Guest Investigators Programs of NASA, as well as the NASA LWS grant NNH08AJ01I.

[26] Zuyin Pu thanks the reviewers for their assistance in evaluating this paper.

References

Albert, J. M. (2003), Evaluation of quasi-linear diffusion coefficients for EMIC waves in a multispecies plasma, *J. Geophys. Res.*, *108*(A6), 1249, doi:10.1029/2002JA009792.

Anderson, B. J., R. E. Denton, G. Ho, D. C. Hamilton, S. A. Fuselier, and F. J. Strangeway (1996), Observational test of local proton cyclotron instability in the Earth's magnetosphere, *J. Geophys. Res.*, *101*, 21,527–21,543, doi:10.1029/96JA01251.

Bossen, M., R. L. McPherron, and C. T. Russell (1976), A statistical study of Pc 1 magnetic pulsations at synchronous orbit, *J. Geophys. Res.*, *81*, 6083–6091, doi:10.1029/JA081i034p06083.

Denton, M. H., M. F. Thomsen, H. Korth, S. Lynch, J. C. Zhang, and M. W. Liemohn (2005), Bulk plasma properties at geosynchronous orbit, *J. Geophys. Res.*, *110*, A07223, doi:10.1029/2004JA010861.

Denton, M. H., J. E. Borovsky, R. M. Skoug, M. F. Thomsen, B. Lavraud, M. G. Henderson, R. L. McPherron, J. C. Zhang, and M. W. Liemohn (2006), Geomagnetic storms driven by ICME- and CIR-dominated solar wind, *J. Geophys. Res.*, *111*, A07S07, doi:10.1029/2005JA011436.

Engebretson, M. J., et al. (2008), Pc1-Pc2 waves and energetic particle precipitation during and after magnetic storms: Superposed epoch analysis and case studies, *J. Geophys. Res.*, *113*, A01211, doi:10.1029/2007JA012362.

Fraser, B. J., and T. S. Nguyen (2001), Is the plasmapause a preferred source region of electromagnetic ion cyclotron waves in the magnetosphere?, *J. Atmos. Sol. Terr. Phys.*, *63*, 1225–1247, doi:10.1016/S1364-6826(00)00225-X.

Gary, S. P. (1993), *Theory of Space Plasma Microinstabilities*, Cambridge Univ. Press, New York.

Gary, S. P., M. B. Moldwin, M. F. Thomsen, D. Winske, and D. J. McComas (1994), Hot proton anisotropies and cool proton temperatures in the outer magnetosphere, *J. Geophys. Res.*, *99*, 23,603–23,615, doi:10.1029/94JA02069.

Gendrin, R., M. Ashour-Abdalla, Y. Omura, and K. Quest (1984), Linear analysis of ion cyclotron interaction in a multicomponent plasma, *J. Geophys. Res.*, *89*, 9119–9124, doi:10.1029/JA089iA10p09119.

Kozyra, J., T. Cravens, A. Nagy, E. Fontheim, and R. Ong (1984), Effects of energetic heavy ions on electromagnetic ion cyclotron wave generation in the plasmapause region, *J. Geophys. Res.*, *89*, 2217–2233, doi:10.1029/JA089iA04p02217.

MacDonald, E. A., M. H. Denton, M. F. Thomsen, and S. P. Gary (2008), Superposed epoch analysis of a whistler instability criterion at geosynchronous orbit during geomagnetic storms, *J. Atmos. Sol. Terr. Phys.*, *70*, 1789–1796, doi:10.1016/j.jastp.2008.03.021.

Meredith, N. P., R. M. Thorne, R. B. Horne, D. Summers, B. J. Fraser, and R. R. Anderson (2003), Statistical analysis of relativistic electron energies for cyclotron resonance with EMIC waves observed on CRRES, *J. Geophys. Res.*, *108*(A6), 1250, doi:10.1029/2002JA009700.

Millan, R. M., and R. M. Thorne (2007), Review of radiation belt relativistic electron losses, *J. Atmos. Sol. Terr. Phys.*, *69*, 362–377, doi:10.1016/j.jastp.2006.06.019.

Miyoshi, Y., and R. Kataoka (2005), Ring current ions and radiation belt electrons during geomagnetic storms driven by coronal mass ejections and corotating interaction regions, *Geophys. Res. Lett.*, *32*, L21105, doi:10.1029/2005GL024590.

O'Brien, T. P., R. L. McPherron, D. Sornette, G. D. Reeves, R. Friedel, and H. J. Singer (2001), Which magnetic storms produce relativistic electrons at geosynchronous orbit?, *J. Geophys. Res.*, *106*, 15,533–15,544, doi:10.1029/2001JA000052.

O'Brien, T. P., K. R. Lorentzen, I. R. Mann, N. P. Meredith, J. B. Blake, J. F. Fennel, M. D. Looper, D. K. Milling, and R. R. Anderson (2003), Energization of relativistic electrons in the presence of ULF wave power and MeV microbursts: Evidence for dual ULF and VLF acceleration, *J. Geophys. Res.*, *108*(A8), 1329, doi:10.1029/2002JA009784.

Reeves, G. D., K. L. McAdams, R. H. W. Friedel, and T. P. O'Brien (2003), Acceleration and loss of relativistic electrons during geomagnetic storms, *Geophys. Res. Lett.*, *30*(10), 1529, doi:10.1029/2002GL016513.

Smith, A. J., N. P. Meredith, and T. P. O'Brien (2004), Differences in ground-observed chorus in geomagnetic storms with and without enhanced relativistic electron fluxes, *J. Geophys. Res.*, *109*, A11204, doi:10.1029/2004JA010491.

Spasojevic, M., H. U. Frey, M. F. Thomsen, S. A. Fuselier, S. P. Gary, B. R. Sandel, and U. S. Inan (2004), The link between a detached subauroral proton arc and a plasmaspheric plume, *Geophys. Res. Lett.*, *31*, L04803, doi:10.1029/2003GL018389.

Summers, D., and R. M. Thorne (2003), Relativistic electron pitch-angle scattering by electromagnetic ion cyclotron waves during geomagnetic storms, *J. Geophys. Res.*, *108*(A4), 1143, doi:10.1029/2002JA009489.

Thomsen, M. F., E. Noveroske, J. E. Borovsky, and D. J. McComas (1999), Calculation of moments from measurements by the Los Alamos Magnetospheric Plasma Analyzer, *LA Rep. LA-13566-MS*, Los Alamos Natl. Lab., Los Alamos, N. M.

L. W. Blum and H. E. Spence, Astronomy Department, Boston University, 725 Commonwealth Avenue, Boston, MA 02215, USA. (lwblum@bu.edu)

S. P. Gary, E. A. MacDonald, and M. F. Thomsen, Los Alamos National Laboratory, P.O. Box 1663, MS D466, Los Alamos, NM 87544, USA.